Article

Density-Functional Tight-Binding Study of Carbonaceous Species Diffusion on the (100)-γ-Al₂O₃ Surface

Aditya W. Sakti, Chien-Pin Chou, and Hiromi Nakai*

Read Online

ACCESS | Metrics & More | Article Recommendations

ABSTRACT: Carbonaceous or oxy-carbon species are intermediates formed during C_xH_y combustion on a Pt_n/Al_2O_3 catalyst, which contain carbon, hydrogen, and oxygen atoms. The accumulation of the carbonaceous species, arguably, leads to catalytic deactivation; therefore, their removal is of importance. As the diffusion process is occasionally the rate-determining step in the growth of carbonaceous species, the present study aims to reveal the diffusion mechanisms. The free energy barriers of acetate, formate, and methoxy diffusion on the (100)-γ-Al₂O₃ surface were evaluated through extensive metadynamics simulations at the density-functional tight-binding level. The present work deduces that each adopted carbonaceous species exhibits different diffusion mechanisms and supports experimental evidence that the acetate species exhibits the slowest diffusivity among the adopted carbonaceous species.
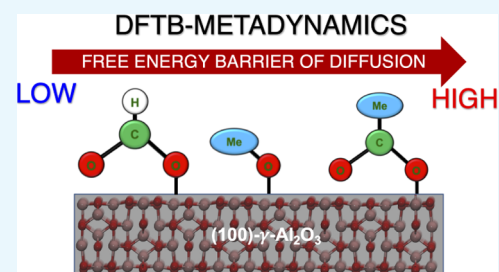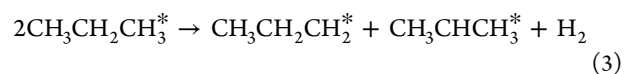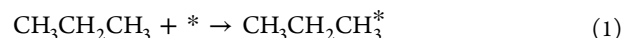
1. INTRODUCTION

The three-way catalyst (TWC) technology is among the innovative catalyst technologies for eliminating the generated hazardous exhaust gases, that is, carbon monoxide (CO), nitrogen oxides (NO_x), and unburnt hydrocarbons (C_xH_y) from vehicles.[1−3] The catalysts are composed of, and not limited to, noble metals (Pt, Pd, or Rh) and metal oxides. The commonly used metal oxides that support TWC are alumina (Al_2O_3),[4−7] zirconia (ZrO_2),[8−12] and ceria (CeO_2).[13−17] Experimental[18−20] and theoretical[21−24] studies were performed extensively for exploring the catalytic activity and elucidating the reaction mechanism.[22,23] During the removal process, CO and C_xH_y are oxidized into CO_2, whereas NO_x is reduced to N_2.[25] In such reactions, the C_xH_y oxidation leads to the formation of intermediates reported in ref 26, namely, oxygenated carbonaceous (oxy-carbon) species. The oxy-carbon intermediates are mainly accumulated on the Al_2O_3 surface.[26] The role of the oxy-carbon species is questionable. However, it has been presumed that the oxy-carbons only act as inert spectators during the oxidation reaction.[26] An experimental study was performed to investigate oxy-carbon growth on a metal oxide surface.[26]

The growth of the oxy-carbon species was observed by diffuse reflectance infrared Fourier-transform spectroscopy coupled with Fourier-transform infrared spectroscopy.[26] The same technique has been used extensively for investigating oxidation over various catalysts, namely, $Pd/CeO_2/Al_2O_3$,[27] Pt/Al_2O_3,[28−30] $Pt/WO_x/Al_2O_3$,[28] $MgCr_2O_4$,[31,32] Co_3O_4,[32] CuO,[32] and $Pt/CeO_2−ZrO_2$.[33] The oxy-carbon species observed on the support materials include acetate ($CH_3COO^−$),[28,31,32] formate ($HCOO^−$),[27,28,31,32] alkoxy ($RO^−$),[32] carbonate ($CO_3^{2−}$),[27−29,33] bicarbonate ($HCO_3^−$),[33]

acetone,[31,32] and unidentified species.[30] The unidentified species was detected when the experiment was conducted in the presence of the SO_2 gas. Temperature-programmed oxidation (TPO) successfully elucidated the composition, location, reactivity, and the role of the oxy-carbon species in hydrocarbon oxidation.[34] The catalytic activity of the supported nanoparticles was also influenced by the kinetics of the TPO process, where the activity increased as the diffusion barrier decreased.[34]

Based on the previous experimental study in ref 26, the reactions represented in eqs 1−8 are plausible elementary reactions for the formation of the oxy-carbon species, where * denotes the active site of the surface. No observation was made to elaborate where the reactions were occurring. Assuming that all the processes occur on the metal nanocluster surface, the oxy-carbon species would spill over on the γ-Al₂O₃ surface.

$$CH_3CH_2CH_3 + * \rightarrow CH_3CH_2CH_3^* \tag{1}$$

$$O_2 + * \rightarrow O_2^* \tag{2}$$

$$2CH_3CH_2CH_3^* \rightarrow CH_3CH_2CH_2^* + CH_3CHCH_3^* + H_2 \tag{3}$$

$$CH_3CH_2CH_2^* + CH_3CHCH_3^* \rightarrow 2CH_3CH{=}CH_2^* + H_2 \quad (4)$$

$$2O_2^* + 2CH_3CH{=}CH_2^* + * \rightarrow CH_3COO^* + HCOO^* + 2H^* \quad (5)$$

$$O_2^* + CH_3CH{=}CH_2^* \rightarrow CH_3O^* + CH_2{=}CHO^* \quad (6)$$

$$O_2^* + CH_3CH_2CH_2^* + 2H^* \rightarrow CH_2{=}CH_2^* + H_2O^* + CH_3O^* + * \quad (7)$$

$$HCOO^* + O_2^* + H_2 \rightarrow HCO_3^* + H_2O^* \quad (8)$$
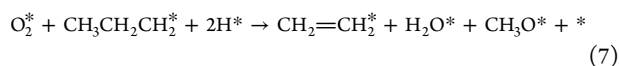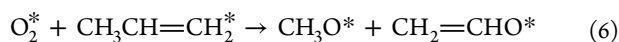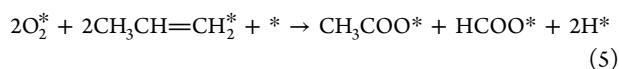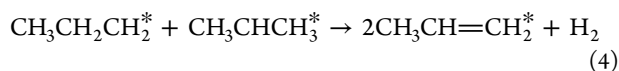
The previous experimental study showed that it is more difficult to oxidize acetate species than the alkoxy and ketone derivatives.[26,34] It was further confirmed that the diffusion of oxy-carbon species plays an important role in the removal process, as diffusion is the rate-determining step of oxy-carbon oxidation.[34] Motivated by the aforementioned experimental facts, in the present theoretical study, the diffusion process of oxy-carbon species was elucidated via molecular dynamics simulations at the density-functional tight-binding (DFTB) level.[35−38] Molecular details on the diffusion mechanism and the surface driving force γ-Al$_2$O$_3$ were investigated.

2. COMPUTATIONAL DETAILS

All DFTB calculations were performed using an in-house code DC-DFTBMD program,[39,40] whereas the reference calculations were performed at the density-functional theory (DFT) level using the Vienna ab Initio Simulation Package (VASP).[41,42] The DFTB calculation was performed using the third-order variant (DFTB3) with the modified parameter set made using the automatized DFTB parameterization toolkit,[43] hereafter called the Al$_2$O$_3$ parameter. As a reference, the calculations were also performed at the DFT level using the generalized-gradient approximation functional, Perdew−Burke−Ernzerhof, revised for solids (PBEsol).[44] To describe the dispersion interaction between the oxy-carbon and the γ-Al$_2$O$_3$ surface, the DFT-D3 dispersion correction with Becke−Johnson damping was employed in both DFTB and DFT calculations.[45] The initial structure of the bulk γ-Al$_2$O$_3$ was reconstructed based on the information obtained from refs 46 and 47. The chosen initial structure is a nonspinel type that has been extensively studied in some previous works.[24,48−53]

First, the initial geometry of the bulk Al$_2$O$_3$ was optimized at the DFT and DFTB levels. The lattice parameters and the optimized geometries were considered for generating the slab structures. The (100)-γ-Al$_2$O$_3$ slabs were generated by cutting the atoms along the (100) plane. Two slab models with different sizes that consist of 160 and 960 atoms, respectively, are shown in Figure 1. To overcome the computational cost for a large system, the divide-and-conquer (DC) option in the DCDFTBMD program was enabled.[39,40,54,55] The subsystems were created automatically using the cubic grid with dimensions of 3 × 3 × 3 Å^3. A buffer radius of 6 Å was used to adjust the accuracy to the same level as the conventional DFTB method.

During the geometry optimization, three-bottom layers of the slab were fixed, while other atoms were relaxed. The oxy-carbon intermediates, namely, methoxy (CH$_3$O$^-$), bicarbonate (HCO$_3^-$), formate (HCOO$^-$), acetate (CH$_3$COO$^-$), and propionate (CH$_3$CH$_2$COO$^-$) were attached on the slab surface. In each prepared structure, oxygen atoms of the oxy-carbon are bound to aluminum atoms, such that they form an
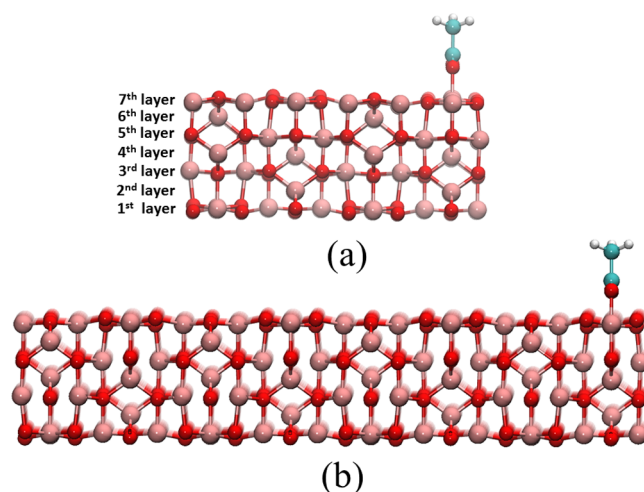
Figure 1. Representative (a) small and (b) large-size slab models adopted in the present work.

octahedral geometry centered at the aluminum atom. The adsorption energies between the oxy-carbon and (100)-γ-Al$_2$O$_3$ slab were calculated at the DFT and DFTB levels with the following formula

$$\Delta E_{ads} = E_{ads} - E_{slab} - E_{carb} \quad (9)$$

E_{ads}, E_{slab}, and E_{carb} represent the total energies of the adsorbed system, slab, and oxy-carbon species, respectively.

The adsorption energies calculated at the DFTB level were compared to the reference calculations at the DFT level. After confirming the parameter accuracy in describing the binding energy, the optimized adsorbed structures were used for MD simulations. At first, the equilibrations were performed under the canonical (NVT) ensemble at the DFTB3-D3(BJ) level for 20 ps with a time step of 1.0 fs to integrate the equation of motion. The equilibrated structures with the details summarized in Table 1 were adopted for further production

Table 1. Slab Size, Adsorbate, Surface Coverage, Number of Adsorbed Oxy-Carbon Species, and Total Number of Atoms of the Adopted Systems

slab size	adsorbate	surface coverage [%]	$N_{oxy\text{-}carbon}$	N_{atoms}
small	CH$_3$COO$^-$	5.00	1	167
small	HCOO$^-$	5.00	1	164
small	CH$_3$O$^-$	2.50	1	165
large	CH$_3$COO$^-$	0.83	1	967
large	CH$_3$COO$^-$	1.67	2	974
large	CH$_3$COO$^-$	9.17	11	1037

runs via the metadynamics sampling scheme.[56−59] The surface coverages listed in Table 1 are calculated based on eq 10.

Surface coverage

$$= \frac{\text{number of oxygen atoms in the oxy-carbon species}}{\text{number of surface atoms}}$$

$$\times 100\% \quad (10)$$

Under the metadynamics scheme, the Al−O coordination number, as formulated in eq 11, was chosen as the collective variable.

Table 2. Comparison of Cell Parameters, Optimized at Different DFT Functionals, and the DFTB Method

method	PBEsol	PBEPBE[a]	M11-L[a]	MN12-L[a]	PW91[b]	DFTB3	DFTB3-D3(BJ)
a [Å]	5.466	5.648	5.491	5.559	5.587	5.570	5.533
b [Å]	8.245	8.528	8.285	8.364	8.413	8.427	8.378
c [Å]	7.956	8.241	8.029	8.097	8.068	7.897	7.865
β [deg]	90.76	91.00	91.24	91.28	90.59	89.46	90.66
volume [Å^3/Al$_2$O$_3$]	44.75	49.61	45.65	47.05	47.40	46.33	45.58
volume deviation [%][c]	−3.54	6.94	−1.60	1.42	2.18	−0.13	−1.75

[a]Calculated results from ref 61. [b]VASP calculations, using the plane wave basis from ref 47. [c]The deviations were calculated relative to the experimental volume of 46.39 Å^3/Al$_2$O$_3$ (ref 62.)
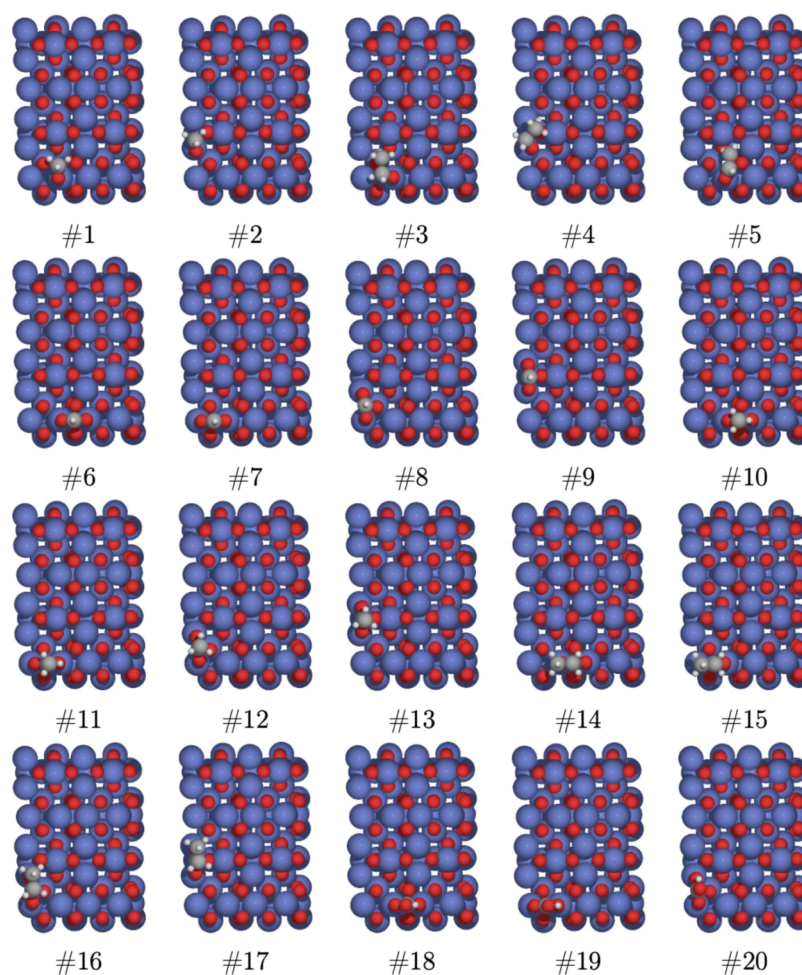

Figure 2. Adsorbed methoxy (#1−#2), ethoxy (#3−#5), formate (#6−#9), acetate (#10−#13), propionate (#14−#17), and bicarbonate (#18−#20) species on (100)-γ-Al$_2$O$_3$ obtained from geometry optimizations at the DFTB3-D3(BJ) level.

$$n_{Al-O} = \sum_{i=1}^{N_O} \sum_{i=j}^{N_{Al}} \frac{\left(1 - \frac{r_{ij}}{r_0}\right)^6}{\left(1 - \frac{r_{ij}}{r_0}\right)^{12}}$$

(11)

r_{ij} and r_0 denote the Al−O distance and cutoff radius, respectively. The value $r_0 = 1.9$ Å was specified to smoothly define Al−O bond breaking and formation during the metadynamics simulations. The Gaussian bias potential with a height of 1.88 kcal/mol and a width of 0.1 (dimensionless, as the coordination number was chosen as the collective variable) was added every 40 fs. The simulations were performed until the estimated free energy barriers converged. The free energy barriers converged after performing 9 metadynamics trajecto-ries with a simulation length of 60 ps. The free energy surfaces were reconstructed by estimating the unbiased probability density function via the weighted histogram analysis method.[60]

3. RESULTS AND DISCUSSION

3.1. Structural Property of Bulk γ-Al$_2$O$_3$. The cell parameters of the optimized bulk structure are listed in Table 2. All DFT functionals fairly reproduce the experimental cell volumes. The PBEPBE functional shows the largest deviation of 6.94% with a volume of 49.61 Å^3, while the experimental cell volume is 46.39 Å^3. Other functionals, such as PBEsol, M11-L, MN12-L, and PW91, exhibit smaller volume deviations of −3.54, −1.60, 1.42, and 2.18%, respectively. The DFTB variants also show smaller volume deviations, namely, −0.13

and −1.74%, for the DFTB3 and DFTB3-D3(BJ) methods, respectively. Despite the volume deviation, the dispersion correction is important for describing weak interactions between oxy-carbon moieties.

3.2. Adsorption of Oxy-Carbon Species on the (100) Surface of γ-Al$_2$O$_3$. The oxy-carbon species or carbonaceous species was deposited on the (100)-γ-Al$_2$O$_3$ surface, which was formed after the spillover process. The optimized geometries of the oxy-carbon species adsorbed on the (100)-γ-Al$_2$O$_3$ surface, namely, methoxy (#1−#2), ethoxy (#3−#5), formate (#6−#9), acetate (#10−#13), propionate (#14−#17), and bicarbonate (#18−#20) are shown in Figure 2.

The calculated adsorption energies (ΔE_{ads}) for the acetate, formate, and methoxy species on (100)-γ-Al$_2$O$_3$ are shown in Table 3. The DFTB method predicts shorter O−Al bond

Table 3. Calculated Adsorption Energies and O−Al Bond Distances for Acetate, Formate, and Methoxy on the (100)-γ-Al$_2$O$_3$ Surface[a] without Dispersion Correction

		r_{O-Al} [Å]		E_{ads}[eV]	
entry	oxy-carbon	PBEsol	DFTB3[b]	PBEsol	DFTB3[b]
#1	methoxy	1.84	1.79 (−0.05)	−1.36	−1.40 (−0.04)
#2	methoxy	1.89	1.81 (−0.08)	−0.96	−0.94 (+0.02)
#3	ethoxy	1.84	1.77 (−0.07)	−1.22	−1.38 (−0.16)
#4	ethoxy	1.90	1.82 (−0.08)	−0.94	−0.91 (+0.04)
#5	ethoxy	1.90	1.82 (−0.08)	−1.09	−1.17 (−0.08)
#6	formate	1.91	1.81 (−0.10)	−0.98	−0.90 (+0.09)
#7	formate	1.89	1.86 (−0.04)	−1.23	−1.07 (+0.16)
#8	formate	1.90	1.86 (−0.04)	−0.98	−0.79 (+0.19)
#9	formate	1.93	1.85 (−0.08)	−0.84	−0.74 (+0.10)
#10	acetate	1.90	1.81 (−0.09)	−0.96	−0.98 (−0.02)
#11	acetate	1.88	1.86 (−0.02)	−1.21	−1.15 (+0.07)
#12	acetate	1.88	1.86 (−0.02)	−0.95	−0.87 (+0.09)
#13	acetate	1.92	1.85 (−0.07)	−0.80	−0.81 (−0.01)
#14	propionate	1.90	1.81 (−0.09)	−0.99	−0.91 (+0.08)
#15	propionate	1.88	1.85 (−0.03)	−1.24	−1.08 (+0.16)
#16	propionate	1.88	1.85 (−0.03)	−0.99	−0.80 (+0.19)
#17	propionate	1.92	1.84 (−0.08)	−0.83	−0.75 (+0.08)
#18	bicarbonate	1.90	1.81 (−0.09)	−1.01	−1.18 (−0.17)
#19	bicarbonate	1.88	1.86 (−0.02)	−1.26	−1.34 (−0.08)
#20	bicarbonate	1.89	1.86 (−0.03)	−1.01	−1.07 (−0.06)
	MAD		0.06		0.09

[a]Herein, the O atom refers to the one that belongs to the oxy-carbon species. The calculations were performed without dispersion correction. [b]Differences from the PBEsol method are shown in parentheses.

lengths with a mean average deviation (MAD) of 0.06 Å, relative to the bond lengths obtained at the PBEsol level. Despite such short bond distances, the calculated ΔE_{ads} at the DFTB level are smaller than those calculated at the DFT level. The adsorption energies are also well reproduced with a MAD of 0.09 eV (2.08 kcal/mol). Such a deviation is under the level of accuracy of the DFTB method as reported in previous works.[63−67] Inclusion of the dispersion correction to both DFT and DFTB calculations also leads to the same MAD as shown in Table 4.

Based on Table 4, the calculated E_{ads} values strongly depend on the location where the oxy-carbon is adsorbed on the surface. According to the estimated E_{ads} values at the DFTB level, the tendency of the oxy-carbon adsorbed on the surface of (100)-γ-Al$_2$O$_3$ is ethoxy ≈ methoxy > bicarbonate >

propionate ≈ formate > acetate. Such an order suggests that removing the acetate species from the surface is energetically easier than that of the formate and methoxy species. However, despite this the acetate species exhibits the smallest adsorption energy, it does not mean that it is easier to be removed from the surface. Because one acetate molecule is adsorbed to the surface via two O−Al bonds, a complete acetate removal requires dissociation of those bonds. Therefore, a more thorough analysis on the free energy of diffusion in the next subsection is of importance to further determine which oxy-carbon species is easier to be removed from the surface.

3.3. Diffusion of Acetate, Formate, and Methoxy Species on the (100) Surface of γ-Al$_2$O$_3$. Snapshots of acetate, formate, and methoxy diffusion are shown in Figure 3. Initially, the oxygen from the acetate, formate, and methoxy was attached on the aluminum atom of the (100)-γ-Al$_2$O$_3$ surface. For the case of acetate and formate, the O−Al bond dissociation retains another O−Al bond on the surface. As a result, the remaining O−Al bond becomes flexible and thus it performs a rotation that enables the oxygen atom of the carbonyl group to interact with another empty orbital of the aluminum atom. As the rotation that took place occurred right after the bond dissociation, the process is analogous to ballet.

Similar to the case of the acetate diffusion mechanism, in the beginning, O−Al, the bond between formate and the (100)-γ-Al$_2$O$_3$, was dissociated. Unlike the case of acetate, where oxygen is the only atom that can interact with the surface, herein, the hydrogen atom has a tendency to interact with the surface oxygen atoms. Such an interaction is slightly weaker with a bond length of 1.82 Å, whereas the O−Al bond length between formate and the surface is 1.75 Å. Once the H−O interaction is complete, the formate moiety is destabilized, leading to the dissociation of the second O−Al. Therefore, generally, formate diffusion is facilitated by a ballet jumping motion that originates from the formation of the H−O bond.

In contrast with the acetate and formate cases, the methoxy radical has only one O−Al bond with the (100)-γ-Al$_2$O$_3$ surface. As shown in Figure 3c, at first, the radical rotates until it finds a good conformation to promote O−Al bond dissociation. Once it is detached from the surface, it performs a random vehicular diffusion[68,69] until a proper orientation is identified for it to be re-adsorbed on to the surface. The random motion on the surface increases the degree of freedom, in particular, for reorienting and forming the O−Al bond.

To further investigate these three mechanisms, the free energy diffusion surfaces were re-constructed and are shown in Figure 4. The free energy barriers, $\Delta F^{\ddagger}$, are summarized in Table 5. As shown in Figure 4a, there are two activated complexes formed during acetate diffusion, with diffusion barriers of 8.01 and 25.31 kcal/mol, respectively. These transition states refer to the dissociation of the O−Al bonds, indicating that each O−Al bond has a different strength, with a ratio $\Delta F^{\ddagger}_{f2}/\Delta F^{\ddagger}_{f1}$ of 3.16. A lower $\Delta F^{\ddagger}_{f2}/\Delta F^{\ddagger}_{f1}$ ratio represents faster diffusivity as the second bond dissociation O−Al is the rate-determining step of the overall diffusion process. On the other hand, owing to the dissociations facilitated by the H−O surface interaction, the formate diffusion exhibits a lower $\Delta F^{\ddagger}_{f2}/\Delta F^{\ddagger}_{f1}$ of 1.90, leading to faster diffusivity than the acetate radical. The third step of formate diffusion involves the dissociation of a relatively weak H−O bond, which is represented by a low free energy barrier of 5.73 kcal/mol.

As described above for the case of methoxy diffusion, only one O−Al bond was dissociated with a moderately high free

Table 4. Calculated Adsorption Energies and O−Al and the Acetate, Formate, and Methoxy Bond Distances on the (100)-γ-Al₂O₃ Surface[a] with Dispersion Correction

entry	oxy-carbon	r_{O-Al} [Å]		E_{ads} [eV]	
		PBEsol-D3(BJ)	DFTB3-D3(BJ)[b]	PBEsol-D3(BJ)	DFTB3-D3(BJ)[b]
#1	methoxy	1.84	1.80 (−0.05)	−1.57	−1.62 (−0.05)
#2	methoxy	1.90	1.83 (−0.07)	−1.15	−1.20 (−0.05)
#3	ethoxy	1.84	1.78 (−0.06)	−1.52	−1.69 (−0.17)
#4	ethoxy	1.89	1.82 (−0.07)	−1.16	−1.20 (−0.04)
#5	ethoxy	1.91	1.82 (−0.09)	−1.08	−1.03 (+0.06)
#6	formate	1.89	1.86 (−0.03)	−1.32	−1.20 (+0.12)
#7	formate	1.90	1.86 (−0.04)	−1.08	−0.93 (+0.14)
#8	formate	1.93	1.86 (−0.08)	−0.93	−0.85 (+0.08)
#9	formate	1.90	1.82 (−0.08)	−1.33	−1.28 (+0.05)
#10	acetate	1.88	1.85 (−0.03)	−1.08	−1.10 (−0.03)
#11	acetate	1.88	1.85 (−0.03)	−1.08	−1.00 (+0.08)
#12	acetate	1.92	1.85 (−0.07)	−0.92	−0.93 (−0.01)
#13	acetate	1.90	1.81 (−0.09)	−1.13	−1.05 (+0.08)
#14	propionate	1.88	1.85 (−0.03)	−1.38	−1.22 (+0.15)
#15	propionate	1.88	1.85 (−0.03)	−1.13	−0.95 (+0.18)
#16	propionate	1.91	1.85 (−0.07)	−0.97	−0.87 (+0.10)
#17	propionate	1.91	1.81 (−0.10)	−1.12	−1.30 (−0.18)
#18	bicarbonate	1.88	1.85 (−0.03)	−1.36	−1.46 (−0.10)
#19	bicarbonate	1.89	1.85 (−0.04)	−1.12	−1.20 (−0.08)
#20	bicarbonate	1.92	1.85 (−0.07)	−0.96	−1.12 (−0.16)
	MAD		0.06		0.09

[a]Herein, the O atom refers to the one that belongs to the oxy-carbon species. All calculations were performed with the DFT-D3(BJ) dispersion correction. [b]Differences from the PBEsol method are shown in parentheses.

energy barrier of 15.46 kcal/mol. The $\Delta F_{f1}^{\ddagger}$ of methoxy diffusion is higher than that of formate diffusion, but still lower than that of acetate. As the methoxy radical performs Brownian diffusion before it is re-adsorbed to the surface, the transition state becomes broader with a few noises as the marks of the small vehicular diffusion barrier. The Brownian diffusion is rather random; therefore, the free energy barrier for methoxy diffusion hardly converges, that is, with a standard deviation of 2.5 kcal/mol.

Note that the $\Delta F^{\ddagger}$ values listed in Table 5 are in the range of experimental values, namely, 5.74−26.05 kcal/mol.[34,70−72] Moreover, in agreement with the TPO experiment, removing acetate radicals is more difficult compared to removing enolate, aliphatic ester, and acetone.[34] Based on the MD simulation at the DFTB level, for the case of the acetate radical, the surface atom configuration, in particular, surface O−Al−O angles where the oxy-carbon was adsorbed (α and β), is primarily responsible for the O−Al bond dissociation. As shown in Figure 5a,b, when the O−Al bond dissociates, namely, when n_{O-Al} reaches zero, α decreases from 105 to 85°, while β increases from 70 to 85°. On the other hand, for the case of formate as shown in Figure 5c,d, the α and β angles do not change significantly, in particular, α is relatively stable at 82°, while β slightly increases from 84 to 88°. In this case, the surface atoms provided a lower driving force for facilitating formate diffusion. As explained previously, formate diffusion is partly facilitated by the interaction between the hydrogen atom of the formate and the oxygen atom on the surface; hence, the diffusion takes place with less efforts from the surface. In stark contrast, as shown in Figure 5e,f, both, the α and β angles, do not change significantly during methoxy diffusion. Although methoxy diffusion is not the fastest among the adopted oxy-carbon species, the surface atoms have a low contribution to the overall diffusion process.

3.4. Coverage Dependence on the Barriers to Acetate Diffusion.
The surface coverage affects the estimated barriers of acetate diffusion as summarized in Table 6. At a low surface coverage, namely, 0.83%, the free energy barriers for the dissociations of the second and first O−Al bonds are 11.23 and 20.92 kcal/mol, respectively. The first intermediate state, where one O−Al bond remains adsorbed on the surface, is more stable than the initial state, as implied by the backward free energy barrier of 17.79 kcal/mol. The first intermediate state is even more stable than the final state where the remaining O−Al bond is dissociated. Conversely, despite the high free-energy dissociation of the second O−Al bond, the backward reaction requires a lower energy of 5.28 kcal/mol. Hence, the second O−Al bond dissociation is an endergonic process with $\Delta F_{f2} > 0$, which indicates that a larger thermal energy is required to induce spontaneity.

As the surface coverage increases to 1.67%, both $\Delta F_{f1}^{\ddagger}$ and $\Delta F_{f2}^{\ddagger}$ decrease to 4.39 and 14.41 kcal/mol, respectively. Similarly, the barriers for backward processes also decrease to 7.61 and 3.77 kcal/mol. Overall, such changes lead to an increase in the free energy difference for the first dissociation process, namely, −3.22 kcal/mol. This indicates that the dissociation of the first O−Al bond becomes more energy demanding. On the other hand, the dissociation of the second bond requires a lower energy than the one at the coverage of 0.83%, with a free energy difference of 10.64 kcal/mol. Overall, at a surface coverage of 1.67%, a lower temperature will be sufficient to promote the entire diffusion process as the total free energy difference, $\Delta F_{f1} + \Delta F_{f2}$ of 7.42 kcal/mol, is smaller than the one at 0.83% surface coverage, namely, 9.08 kcal/mol. The decrement in ΔF_{f2} helps mitigate the increment in ΔF_{f1}. It is speculated that such decrement stems from the surface deformation when an additional acetate molecule is adsorbed on the surface.
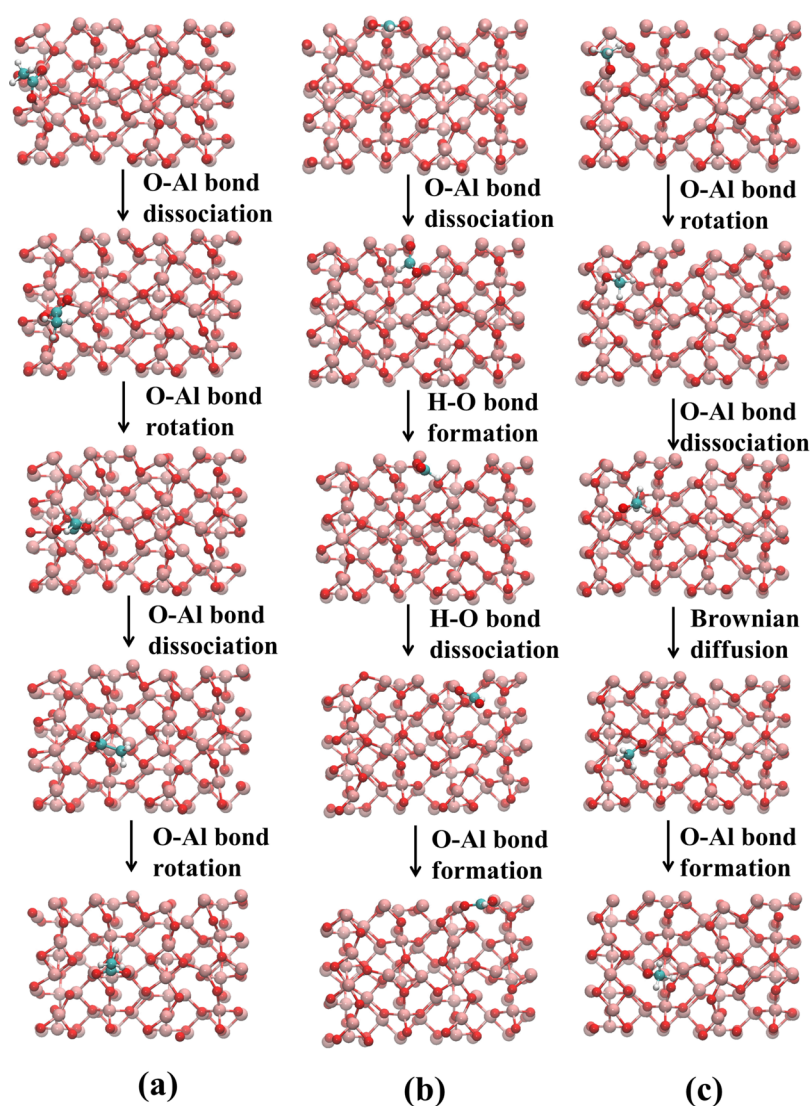
Figure 3. Representative metadynamics snapshots of (a) acetate, (b) formate, and (c) methoxy diffusion on (100)-γ-Al$_2$O$_3$ surface.
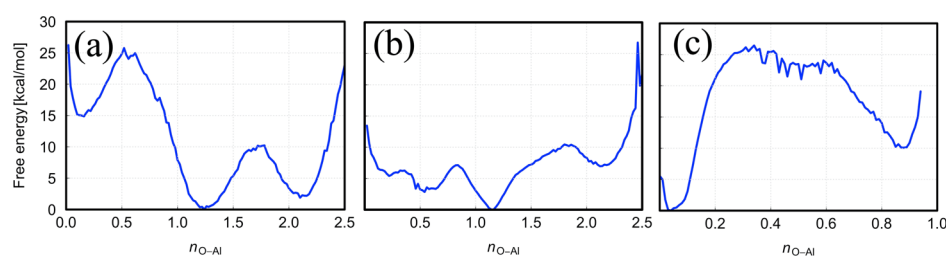

Figure 4. Reconstructed free energy surfaces of (a) acetate, (b) formate, and (c) methoxy diffusion.

Table 5. Estimated Free Energy Barriers of Acetate, Formate, and Methoxy Diffusion on the (100)-γ-Al$_2$O$_3$ Surface in kcal/mol

species	$\Delta F_{f1}^{\ddagger}$	$\Delta F_{f2}^{\ddagger}$	$\Delta F_{f3}^{\ddagger}$	$\Delta F_{f2}^{\ddagger}/\Delta F_{f1}^{\ddagger}$	$\Delta F_{b1}^{\ddagger}$	$\Delta F_{b2}^{\ddagger}$	$\Delta F_{b3}^{\ddagger}$
acetate	8.01	25.31		3.16	9.59	10.97	
formate	6.82	12.95	5.73	1.90	19.28	7.42	1.58
methoxy	15.46				25.45		

When the surface coverage is further increased to 9.17%, the dissociation barriers of the first and second O—Al bonds

slightly increase to 4.61 and 15.29 kcal/mol, respectively. These increments are, however, insignificant, at 0.22 and 0.88 kcal/mol, respectively. Such values are still within the statistical error of metadynamics sampling and re-weighting. In contrast, the backward process for the first dissociation step is reduced significantly from 7.61 to 1.80 kcal/mol. As the backward process is easier, the first dissociation process becomes thermodynamically unfavorable with a free energy difference of 2.80 kcal/mol. The difficulty with dissociating the first O—Al bond may arise from the steric hindrance between the acetate moieties. On the other hand, the second dissociation process is slightly easier than that with a surface coverage of
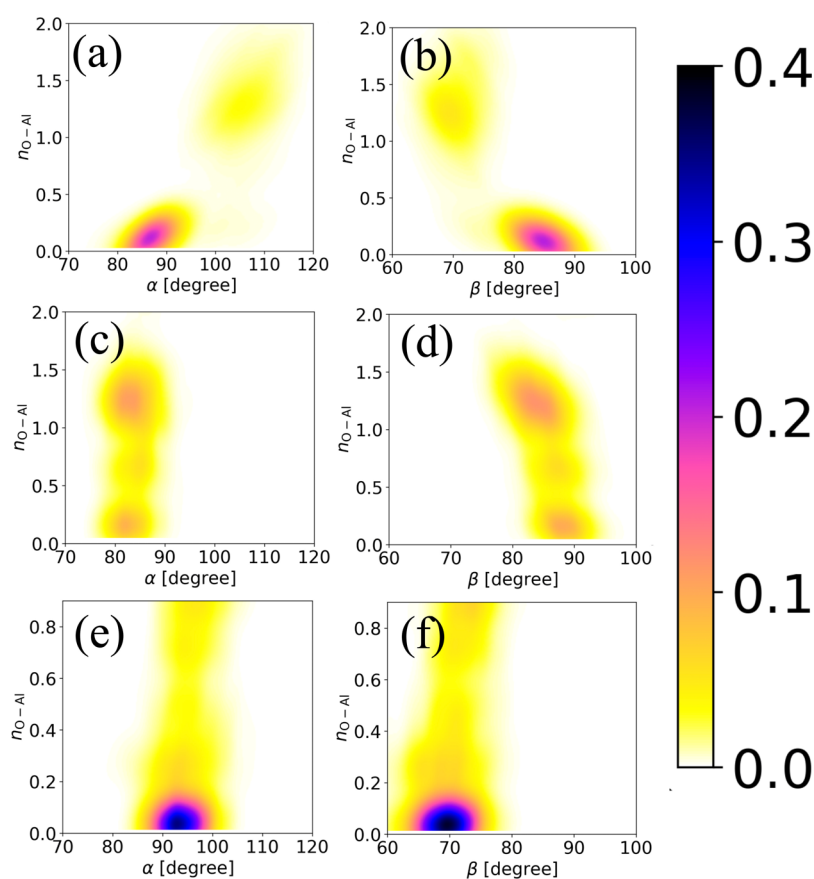
Figure 5. Probability density distribution of the correlation between α and β angles and the coordination number of oxygen atom, n_{O-Al} of acetate (a,b), formate (c,d), and methoxy species (e,f).

Table 6. Estimated Free Energy Barriers ($\Delta F^{\ddagger}$) and Free Energy Differences (ΔF) of Acetate Diffusion at Different Surface Coverage Levels

surface coverage [%]	$\Delta F_{f1}^{\ddagger}$ [kcal/mol]	$\Delta F_{f2}^{\ddagger}$ [kcal/mol]	$\Delta F_{b1}^{\ddagger}$ [kcal/mol]	$\Delta F_{b2}^{\ddagger}$ [kcal/mol]	ΔF_{f1} [kcal/mol]	ΔF_{f2} [kcal/mol]
0.83	11.23	20.92	17.79	5.28	−6.56	15.64
1.67	4.39	14.41	7.61	3.77	−3.22	10.64
9.17	4.61	15.29	1.80	5.92	2.80	9.37

1.67%, with a free energy difference of 9.37 kcal/mol. As acetate diffusion is difficult at 9.17% surface coverage, one needs to control and minimize the growth of the acetate radical on the Al_2O_3 surface.

4. CONCLUSIONS

In conclusion, metadynamics simulations at the DFTB level successfully revealed molecular mechanisms of acetate, formate, and methoxy diffusion on a (100)-γ-Al_2O_3 surface. The present study has examined three diffusion mechanisms that depend on unique interactions between the oxy-carbon radical with the surface. Although acetate and formate have the same functional group, namely, carboxylate (−COO•), they exhibit different diffusion mechanisms. For these carboxylic species, the oxygen atoms were attached asymmetrically, where the O−Al bonds had nonequivalent strength. The acetate diffusion uniquely mimics a ballerina dancer, namely, one O−Al bond rotation occurs immediately after another O−Al bond dissociates. The acetate radical displays the slowest diffusivity among the other oxy-carbon species adopted in the present work. Further investigation shows that the spontaneity of the O−Al bond dissociation is affected by the surface coverage.

Increasing the surface coverage to 9.17% leads to non-spontaneous O−Al bond dissociation. Although further investigation to elucidate this phenomenon has not been carried out, it is speculated that the steric hindrance between acetate residues is at play in suppressing the acetate diffusion. The present work suggests that removing the acetate species from the surface is easier at an early stage of its growth, that is, when the surface coverage less than 9%.

On the other hand, the formate radical exhibits the fastest diffusion by forming the O−H bond between the hydrogen atom of the formate radical with the surface oxygen atom. The nature of its fast diffusion, however, is experimentally unobservable, as the diffusion of the formate radical is indistinguishable among the other oxy-carbon species.[26] The present work suggests that it is easier to remove the formate radical from the (100)-γ-Al_2O_3 surface than the acetate or methoxy species. In contrast to the acetate and formate cases, the methoxy radical performs Brownian diffusion. As only one O−Al bond dissociates, Brownian diffusion occurs right after dissociation. Despite the dissociation of only one O−Al bond, the process is slower than formate diffusion due to the lack of surface deformation during methoxy diffusion. Overall, the

order of diffusivity among the adopted oxy-carbon species is acetate < methoxy < formate. While the order was not experimentally confirmed, it was reported that the acetate radical exhibits the slowest diffusion.[34]

AUTHOR INFORMATION

Corresponding Author

Hiromi Nakai — *Element Strategy Initiative for Catalysts and Batteries (ESICB), Kyoto University, Kyoto 615-8520, Japan; Waseda Research Institute for Science and Engineering (WISE) and Department of Chemistry and Biochemistry, School of Advanced Science and Engineering, Waseda University, Tokyo 169-8555, Japan;* orcid.org/0000-0001-5646-2931; Phone: +81 3-5286-3452; Email: nakai@chem.waseda.jp; Fax: +81 3-3205-2504

Authors

Aditya W. Sakti — *Element Strategy Initiative for Catalysts and Batteries (ESICB), Kyoto University, Kyoto 615-8520, Japan; Waseda Research Institute for Science and Engineering (WISE), Waseda University, Tokyo 169-8555, Japan*

Chien-Pin Chou — *Waseda Research Institute for Science and Engineering (WISE), Waseda University, Tokyo 169-8555, Japan*

Complete contact information is available at:
https://pubs.acs.org/10.1021/acsomega.0c00203

Notes

The authors declare no competing financial interest.

ABBREVIATIONS

MTD, metadynamics; MD, molecular dynamics; DFTB, density-functional tight-binding; DC-DFTB, divide-and-conquer-density-functional tight-binding

REFERENCES

(1) Rainer, D. R.; Koranne, M.; Vesecky, S. M.; Goodman, D. W. CO + O₂ and CO + NO Reactions over Pd/Al₂O₃ Catalysts. *J. Phys. Chem. B* **1997**, *101*, 10769−10774.

(2) Taylor, K. C. Nitric Oxide Catalysis in Automotive Exhaust Systems. *Catal. Rev.* **1993**, *35*, 457−481.

(3) Shelef, M.; Otto, K. Appearance of N₂O in the catalytic reduction of NO by CO. *J. Catal.* **1968**, *10*, 408−412.

(4) Montini, T.; Melchionna, M.; Monai, M.; Fornasiero, P. Fundamentals and Catalytic Applications of CeO₂-Based Materialsr. *Chem. Rev.* **2016**, *116*, 5987−6041.

(5) Koleva, I. Z.; Aleksandrov, H. A.; Vayssilov, G. N. Decomposition behavior of platinum clusters supported on ceria and γ-alumina in the presence of carbon monoxide. *Catal. Sci. Technol.* **2017**, *7*, 734−742.

(6) Trueba, M.; Trasatti, S. P. γ-Alumina as a Support for Catalysts: A Review of Fundamental Aspects. *Eur. J. Inorg. Chem.* **2005**, *2005*, 3393−3403.

(7) Kim, Y. E.; Lee, W.; Youn, M. H.; Jeong, S. K.; Kim, H. J.; Park, J. C.; Park, K. T. Leaching-resistant SnO₂/γ-Al₂O₃ nanocatalyst for stable electrochemical CO₂ reduction into formate. *J. Ind. Eng. Chem.* **2019**, *78*, 73−78.

(8) Zakaria, M. B.; Malgras, V.; Nagata, T.; Kim, J.; Bando, Y.; Fatehmulla, A.; Aldhafiri, A. M.; Farooq, W. A.; Jikihara, Y.; Nakayama, T.; Yamauchi, Y.; Lin, J. Gold nanoparticles anchored on mesoporous zirconia thin films for efficient catalytic oxidation of carbon monoxide at low temperatures. *Microporous Mesoporous Mater.* **2019**, *288*, 109530.

(9) Wang, J.; Wen, J.; Shen, M. Effect of Interaction between Ce₀.₇Zr₀.₃O₂ and Al₂O₃ on Structural Characteristics, Thermal Stability, and Oxygen Storage Capacity. *J. Phys. Chem. C* **2008**, *112*, 5113−5122.

(10) Lin, S.; Yang, L.; Yang, X.; Zhou, R. Redox properties and metal−support interaction of Pd/Ce₀.₆₇Zr₀.₃₃O₂− Al₂O₃ catalyst for CO, HC and NOₓ elimination. *Appl. Surf. Sci.* **2014**, *305*, 642−649.

(11) Lin, S.; Yang, X.; Yang, L.; Zhou, R. Three-way catalytic performance of Pd/Ce₀.₆₇Zr₀.₃₃O₂− Al₂O₃ catalysts: Role of the different Pd precursors. *Appl. Surf. Sci.* **2015**, *327*, 335−343.

(12) Morikawa, A.; Suzuki, T.; Kanazawa, T.; Kikuta, K.; Suda, A.; Shinjo, H. A new concept in high performance ceria−zirconia oxygen storage capacity material with Al₂O₃ as a diffusion barrier. *Appl. Catal. B Environ.* **2008**, *78*, 210−221.

(13) Koga, H.; Hayashi, A.; Ato, Y.; Tada, K.; Hosokawa, S.; Tanaka, T.; Okumura, M. Effect of ceria and zirconia supports on NO reduction over platinum-group metal catalysts: A DFT study with comparative experiments. *Catal. Today* **2019**, *332*, 236−244.

(14) Lan, L.; Wang, J.; Chen, S.; Li, D.; Li, H.; Liu, D.; Wang, W.; Chen, Y. Enhanced activity and hydrothermal stability of Rh-based three-way catalyst for emission control from motorcycles with the assistance of monoethanolamine. *J. Ind. Eng. Chem.* **2019**, *71*, 127−136.

(15) Li, P.; Chen, X.; Li, Y.; Schwank, J. W. A review on oxygen storage capacity of CeO₂-based materials: Influence factors, measurement techniques, and applications in reactions related to catalytic automotive emissions control. *Catal. Today* **2019**, *327*, 90−115.

(16) Kim, J.-R.; Myeong, W.-J.; Ihm, S.-K. Characteristics of CeO₂− ZrO₂ mixed oxide prepared by continuous hydrothermal synthesis in supercritical water as support of Rh catalyst for catalytic reduction of NO by CO. *J. Catal.* **2009**, *263*, 123−133.

(17) Lambrou, P. S.; Efstathiou, A. M. The effects of Fe on the oxygen storage and release properties of model Pd− Rh/CeO₂− Al₂O₃ three-way catalyst. *J. Catal.* **2006**, *240*, 182−193.

(18) Djéga-Mariadassou, G.; Berger, M.; Gorce, O.; Park, J. W.; Pernot, H.; Potvin, C.; Thomas, C.; Da Costa, P. Studies in Surface Science and Catalysis. In *Past and Present in DeNO Catalysis*; Granger, P., Pârvulescu, V. I., Eds.; Elsevier, 2007; Vol. *171*; pp 145−173.

(19) Rogemond, E.; Essayem, N.; Fréty, R.; Perrichon, V.; Primet, M.; Chevrier, M.; Gauthier, C.; Mathis, F. Characterization of Model Three-Way Catalysts: III. Infrared Study of the Surface Composition of Platinum-Rhodium Ceria Alumina Catalysts. *J. Catal.* **1999**, *186*, 414−422.

(20) Chuang, S. S. C.; Tan, C.-D. Combined infrared and mass spectrometric study of reactions of adsorbed NO and CO on 0.5 wt% Rh/SiO₂ catalyst. *Catal. Today* **1997**, *35*, 369−377.

(21) Ishimoto, R.; Jung, C.; Tsuboi, H.; Koyama, M.; Endou, A.; Kubo, M.; Del Carpio, C. A.; Miyamoto, A. Periodic density functional and tight-binding quantum chemical molecular dynamics study of catalytic properties on γ-Al₂O₃ supported Pt catalysts. *Appl. Catal., A* **2006**, *305*, 64−69.

(22) Yang, J.; Wang, H.; Zhao, X.; Li, Y. L.; Fan, W. L. Correlating the surface structure and hydration of a γ-Al₂O₃ support with the Run (n = 1 − 4) cluster adsorption behavior: a density functional theory study. *RSC Adv.* **2016**, *6*, 40459−40473.

(23) Yang, T.; Ehara, M. Probing the electronic structures of Co$_n$ (n = 1 − 5) clusters on γ-Al$_2$O$_3$ surfaces using first-principles calculations. *Phys. Chem. Chem. Phys.* **2017**, *19*, 3679−3687.

(24) Yang, T.; Fukuda, R.; Hosokawa, S.; Tanaka, T.; Sakaki, S.; Ehara, M. A Theoretical Investigation on CO Oxidation by Single-Atom Catalysts M$_1$/γ-Al$_2$O$_3$ (M=Pd, Fe, Co, and Ni). *ChemCatChem* **2017**, *9*, 1222−1229.

(25) Deushi, F.; Ishikawa, A.; Nakai, H. Density Functional Theory Analysis of Elementary Reactions in NO$_x$ Reduction on Rh Surfaces and Rh Clusters. *J. Phys. Chem. C* **2017**, *121*, 15272−15281.

(26) O'Brien, C. P.; Lee, I. C. A detailed spectroscopic analysis of the growth of oxy-carbon species on the surface of Pt/Al$_2$O$_3$ during propane oxidation. *J. Catal.* **2017**, *347*, 1−8.

(27) Faria, W. L. S.; Perez, C. A. C.; César, D. V.; Dieguez, L. C.; Schmal, M. In situ characterizations of Pd/Al$_2$O$_3$ and Pd/CeO$_2$/Al$_2$O$_3$ catalysts for oxidative steam reforming of propane. *Appl. Catal., B* **2009**, *92*, 217−224.

(28) Wu, X.; Zhang, L.; Weng, D.; Liu, S.; Si, Z.; Fan, J. Total oxidation of propane on Pt/WO$_x$/Al$_2$O$_3$ catalysts by formation of metastable Pt$^{δ+}$ species interacted with WO$_x$ clusters. *J. Hazard. Mater.* **2012**, *225−226*, 146−154.

(29) Carlsson, P.-A.; Mollner, S.; Arnby, K.; Skoglundh, M. Effect of periodic operation on the low-temperature activity for propane oxidation over Pt/Al$_2$O$_3$ catalysts. *Chem. Eng. Sci.* **2004**, *59*, 4313−4323.

(30) Hinz, A.; Skoglundh, M.; Fridell, E.; Andersson, A. An Investigation of the Reaction Mechanism for the Promotion of Propane Oxidation over Pt/Al$_2$O$_3$ by SO$_2$. *J. Catal.* **2001**, *201*, 247−257.

(31) Finocchio, E.; Busca, G.; Lorenzelli, V.; Willey, R. J. The Activation of Hydrocarbon CH Bonds over Transition Metal Oxide Catalysts: A FTIR Study of Hydrocarbon Catalytic Combustion over MgCr$_2$O$_4$. *J. Catal.* **1995**, *151*, 204−215.

(32) Finocchio, E.; Willey, R. J.; Busca, G.; Lorenzelli, V. FTIR studies on the selective oxidation and combustion of light hydrocarbons at metal oxide surfaces. *J. Chem. Soc., Faraday Trans.* **1997**, *93*, 175−180.

(33) Wang, B.; Wu, X.; Ran, R.; Si, Z.; Weng, D. IR characterization of propane oxidation on Pt/CeO$_2$− ZrO$_2$: The reaction mechanism and the role of Pt. *J. Mol. Catal. A: Chem.* **2012**, *356*, 100−105.

(34) O'Brien, C. P.; Lee, I. C. Kinetic Modeling of Spillover and Temperature-Programmed Oxidation of Oxy-Carbon Surface Species on Pt/Al$_2$O$_3$. *J. Phys. Chem. C* **2017**, *121*, 12329−12336.

(35) Porezag, D.; Frauenheim, T.; Köhler, T.; Seifert, G.; Kaschner, R. Construction of tight-binding-like potentials on the basis of density-functional theory: Application to carbon. *Phys. Rev. B: Condens. Matter Mater. Phys.* **1995**, *51*, 12947−12957.

(36) Elstner, M.; Porezag, D.; Jungnickel, G.; Elsner, J.; Haugk, M.; Frauenheim, T.; Suhai, S.; Seifert, G. Self-consistent-charge density-functional tight-binding method for simulations of complex materials properties. *Phys. Rev. B: Condens. Matter Mater. Phys.* **1998**, *58*, 7260−7268.

(37) Seifert, G.; Porezag, D.; Frauenheim, T. Calculations of molecules, clusters, and solids with a simplified LCAO-DFT-LDA scheme. *Int. J. Quantum Chem.* **1996**, *58*, 185−192.

(38) Gaus, M.; Cui, Q.; Elstner, M. DFTB3: Extension of the Self-Consistent-Charge Density-Functional Tight-Binding Method (SCC-DFTB). *J. Chem. Theory Comput.* **2011**, *7*, 931−948.

(39) Nishizawa, H.; Nishimura, Y.; Kobayashi, M.; Irle, S.; Nakai, H. Three pillars for achieving quantum mechanical molecular dynamics simulations of huge systems: Divide-and-conquer, density-functional tight-binding, and massively parallel computation. *J. Comput. Chem.* **2016**, *37*, 1983−1992.

(40) Nishimura, Y.; Nakai, H. Dcdftbmd: Divide-and-Conquer Density Functional Tight-Binding Program for Huge-System Quantum Mechanical Molecular Dynamics Simulations. *J. Comput. Chem.* **2019**, *40*, 1538−1549.

(41) Kresse, G.; Furthmüller, J. Efficiency of ab-initio total energy calculations for metals and semiconductors using a plane-wave basis set. *Comput. Mater. Sci.* **1996**, *6*, 15−50.

(42) Kresse, G.; Furthmüller, J. Efficient iterative schemes for ab initio total-energy calculations using a plane-wave basis set. *Phys. Rev. B: Condens. Matter Mater. Phys.* **1996**, *54*, 11169−11186.

(43) Chou, C.-P.; Nishimura, Y.; Fan, C. C.; Mazur, G.; Irle, S.; Witek, H. A. Automatized Parameterization of DFTB Using Particle Swarm Optimization. *J. Chem. Theory Comput.* **2016**, *12* (1), 53−64.

(44) Perdew, J. P.; Ruzsinszky, A.; Csonka, G. I.; Vydrov, O. A.; Scuseria, G. E.; Constantin, L. A.; Zhou, X.; Burke, K. Restoring the density-gradient expansion for exchange in solids and surfaces. *Phys. Rev. Lett.* **2008**, *100*, 136406.

(45) Grimme, S.; Ehrlich, S.; Goerigk, L. Effect of the damping function in dispersion corrected density functional theory. *J. Comput. Chem.* **2011**, *32*, 1456−1465.

(46) Digne, M.; Sautet, P.; Raybaud, P.; Euzen, P.; Toulhoat, H. Hydroxyl Groups on γ-Alumina Surfaces: A DFT Study. *J. Catal.* **2002**, *211*, 1−5.

(47) Digne, M.; Sautet, P.; Raybaud, P.; Euzen, P.; Toulhoat, H. Use of DFT to achieve a rational understanding of acid−basic properties of γ-alumina surfaces. *J. Catal.* **2004**, *226*, 54−68.

(48) Valero, M. C.; Raybaud, P.; Sautet, P. Nucelation of Pd$_n$ (n = 1 − 5) clusters and wetting of Pd particles on γ Al$_2$O$_3$ surfaces: A density functional theory study. *Phys. Rev. B: Condens. Matter Mater. Phys.* **2007**, *75*, 045427.

(49) Shi, X.-R.; Sholl, D. S. Nucleation of Rh$_n$ (n = 1 − 5) Clusters on γ-Al$_2$O$_3$ Surfaces: A Density Functional Theory Study. *J. Phys. Chem. C* **2012**, *116*, 10623−10631.

(50) Wang, Y.; Su, Y.; Kang, L. Stability and nucleation of Ir$_n$ (n = 1 − 5) clusters on different γ-Al$_2$O$_3$ surfaces: A density functional theory study. *Phys. Lett. A* **2016**, *380*, 718−725.

(51) Liu, Z.; Wang, Y.; Li, J.; Zhang, R. The effect of γ-Al$_2$O$_3$ surface hydroxylation on the stability and nucleation of Ni in Ni/γ-Al$_2$O$_3$ catalyst: a theoretical study. *RSC Adv.* **2014**, *4*, 13280−13292.

(52) Liu, Y.; Cen, W.; Feng, G.; Chu, Y.; Kong, D.; Yin, H. First principles study on the adsorption of Pt$_n$ (n = 1 − 4) on γ-Al$_2$O$_3$(110) surface. *Appl. Surf. Sci.* **2014**, *313*, 424−431.

(53) Li, J.; Zhang, R.; Wang, B. Influence of the hydroxylation of γ-Al$_2$O$_3$ surfaces on the stability and growth of Cu for Cu/γ-Al$_2$O$_3$ catalyst: A DFT study. *Appl. Surf. Sci.* **2013**, *270*, 728−736.

(54) Kobayashi, M.; Nakai, H. How does it become possible to treat delocalized and/or open-shell systems in fragmentation-based linear-scaling electronic structure calculations? The case of the divide-and-conquer method. *Phys. Chem. Chem. Phys.* **2012**, *14*, 7629−7639.

(55) Nishimura, Y.; Nakai, H. Parallel implementation of efficient charge-charge interaction evaluation scheme in periodic divide-and-conquer density-functional tight-binding calculations. *J. Comput. Chem.* **2018**, *39*, 105−116.

(56) Laio, A.; Rodriguez-Fortea, A.; Gervasio, F. L.; Ceccarelli, M.; Parrinello, M. Assessing the Accuracy of Metadynamics. *J. Phys. Chem. B* **2005**, *109*, 6714−6721.

(57) Iannuzzi, M.; Laio, A.; Parrinello, M. Efficient Exploration of Reactive Potential Energy Surfaces Using Car-Parrinello Molecular Dynamics. *Phys. Rev. Lett.* **2003**, *90*, 238302.

(58) Laio, A.; Gervasio, F. L. Metadynamics: a method to simulate rare events and reconstruct the free energy in biophysics, chemistry and material science. *Rep. Prog. Phys.* **2008**, *71*, 126601.

(59) Laio, A.; Parrinello, M. Escaping free-energy minima. *Proc. Natl. Acad. Sci. U.S.A.* **2002**, *99*, 12562−12566.

(60) Chodera, J. D.; Swope, W. C.; Pitera, J. W.; Seok, C.; Dill, K. A. Use of the Weighted Histogram Analysis Method for the Analysis of Simulated and Parallel Tempering Simulations. *J. Chem. Theory Comput.* **2007**, *3*, 26−41.

(61) Gu, J.; Wang, J.; Leszczynski, J. Structure and Energetics of (111) Surface of γ-Al$_2$O$_3$: Insights from DFT Including Periodic Boundary Approach. *ACS Omega* **2018**, *3*, 1881−1888.

(62) Wilson, S. J. The dehydration of boehmite, γ-AlOOH, to γ-Al$_2$O$_3$. *J. Solid State Chem.* **1979**, *30*, 247−255.

(63) Addicoat, M. A.; Stefanovic, R.; Webber, G. B.; Atkin, R.; Page, A. J. Assessment of the Density Functional Tight Binding Method for Protic Ionic Liquids. *J. Chem. Theory Comput.* **2014**, *10*, 4633−4643.

(64) Liang, R.; Swanson, J. M. J.; Voth, G. A. Benchmark Study of the SCC-DFTB Approach for a Biomolecular Proton Channel. *J. Chem. Theory Comput.* **2014**, *10*, 451−462.

(65) Settergren, N. M.; Bühlmann, P.; Amin, E. A. Assessment of Density Functionals, Semiempirical Methods, and SCC-DFTB for Protonated Creatinine Geometries. *Theochem* **2008**, *861*, 68−73.

(66) Oliveira, A. F.; Seifert, G.; Heine, T.; Duarte, H. A. Density-functional based tight-binding: an approximate DFT method. *J. Braz. Chem. Soc.* **2009**, *20*, 1193−1205.

(67) Zheng, G.; Irle, S.; Morokuma, K. Performance of the DFTB method in comparison to DFT and semiempirical methods for geometries and energies of C_{20}−C_{86} fullerene isomers. *Chem. Phys. Lett.* **2005**, *412*, 210−216.

(68) Toro-Mendoza, J.; Rodriguez-Lopez, G.; Paredes-Altuve, O. Brownian diffusion of a particle at an air/liquid interface: the elastic (not viscous) response of the surface. *Phys. Chem. Chem. Phys.* **2017**, *19*, 9092−9095.

(69) Bai, Z.-W.; Ding, L.-P. Surface diffusion of a Brownian particle subjected to an external harmonic noise. *Int. J. Mod. Phys. B* **2017**, *31*, 1750082.

(70) Zhu, N.; Liu, Y.-y.; Wang, Y.; Chen, F.-Q.; Zhan, X.-l. Kinetic Models for the Coke Combustion on Deactivated ZSM-5/MOR Derived from n-Heptane Cracking. *Ind. Eng. Chem. Res.* **2010**, *49*, 89−93.

(71) Mahamulkar, S.; Yin, K.; Agrawal, P. K.; Davis, R. J.; Jones, C. W.; Malek, A.; Shibata, H. Formation and Oxidation/Gasification of Carbonaceous Deposits: A Review. *Ind. Eng. Chem. Res.* **2016**, *55*, 9760−9818.

(72) Li, C.; Minh, C. L.; Brown, T. C. Kinetics of CO and CO_2 Evolution During the Temperature-Programmed Oxidation of Coke Deposited on Cracking Catalysts. *J. Catal.* **1998**, *178*, 275−283.